Zeckendorf representation of multiplicative inverses modulo a Fibonacci number

Materials Characterization 220 (2025) 114697

Contents lists available at ScienceDirect

Materials Characterization

journal homepage: www.elsevier.com/locate/matchar

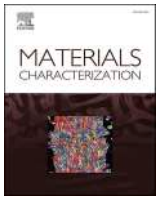

Design optimization for defect-free AISI 316 L/IN718 functionally graded materials produced by laser additive manufacturing

Reza Ghanavati [a,e,f], Homam Naffakh-Moosavy [a,**], Mahmoud Moradi [b], Federico Mazzucato [c], Anna Valente [c], Sara Bagherifard [d], Abdollah Saboori [e,f,*]

[a] Department of Materials Engineering, Tarbiat Modares University (TMU), PO Box 14115-143, Tehran, Iran
[b] Faculty of Arts, Science and Technology, University of Northampton, Northampton NN1 5PH, UK
[c] Department of Innovative Technologies, University of Applied Science and Arts of Southern Switzerland (SUPSI), Via La Santa 1, 6962 Lugano, Switzerland
[d] Department of Mechanical Engineering, Politecnico di Milano, Via La Masa 1, 20156 Milano, Italy
[e] Department of Management and Production Engineering, Politecnico di Torino, Corso Duca Degli Abruzzi 24, 10129 Torino, Italy
[f] Integrated Additive Manufacturing Center (IAM@PoliTo), Politecnico di Torino, Corso Castelfidardo 51, 10129 Torino, Italy

ARTICLE INFO

Keywords:
Additive manufacturing
FGMs design
Microstructure
Crystallographic texture
Mechanical properties

ABSTRACT

Additive manufacturing (AM) of functionally graded materials (FGM) has become an important growing trend in the research and development of various sectors. The main challenging issue is alloy design for the transition zone between terminal alloys so that the expected performance is achieved with minimal risk of defects. In this study, the transition zone design in AISI 316 L-IN718 FGM via laser-directed energy deposition (L-DED) is investigated concerning susceptibility to cracking defect, its formation mechanisms, as well as the design effect on mechanical properties. Consequently, the compatible design of the AISI 316 L-IN718 graded materials is established for laser-based AM. The evaluation of the gradient structures showed that the 75 % AISI 316 L-25 % IN718 region, with the continuous evolution of low-melting eutectic compounds caused by the formation of crystallographic texture in the build direction, is highly sensitive to liquation cracking, which occurs in the presence of thermal stresses arising from the deposition of subsequent layers. In addition, defects of porosity and oxide micro-inclusions intensify the discontinuity and cracking in the remarked composition region. Finally, it was demonstrated that the improvement of the dissimilar structure of AISI 316 L and IN718 alloys can be purposefully fulfilled by designing a compositional gradient in the form of a 50 wt% mixed region between the base alloys (FGM-50 %) resulted in the maximum mechanical properties (tensile strength 540 ± 10 MPa, elongation 52 ± 2 %, and toughness 24 ± 1.4 kJ/mm^3).

1. Introduction

In recent years, the development of advanced metallic materials through additive manufacturing (AM) technology has been accelerated due to the elimination of the inherent obstacles of conventional manufacturing (CM) methods, the unique capability to directly realize the design into the final part, and the advancement of materials science and metallurgy in AM [1–4]. Functionally graded/gradient materials (FGMs), determined by gradual evolution of their characteristics (such as porosity, microstructure, and composition) in preferred direction(s) to provide site-specific properties, are those advanced engineering materials that the layer-by-layer manner of AM is well suited to their concept as it can place materials in the exact designed position [5,6]. Accordingly, lots of attention has led to the standardization (ISO/ASTM TR 52912) of the production of FGMs by AM, abbreviated as FGAM, and adaptation to high-tech industries [7]. The AM process of directed energy deposition (DED) owing to the powder blowing/wire injection mechanism gives high flexibility to adjust the base materials combination while fabricating complex compositional FGMs, thus it has been much referred to in literature [8,9]. In contrast, the powder bed fusion (PBF) process is of interest for the fabrication of structural FGMs, though recently efforts have been made to enable it in selective powder dispersion and building multi-material [10].

One of the most interesting cases of FGAM is the structure of stainless

* Corresponding author at: Department of Management and Production Engineering, Politecnico di Torino, Corso Duca Degli Abruzzi 24, 10129 Torino, Italy.
** Corresponding author.
E-mail addresses: h.naffakh-moosavy@modares.ac.ir (H. Naffakh-Moosavy), abdollah.saboori@polito.it (A. Saboori).

https://doi.org/10.1016/j.matchar.2024.114697
Received 13 October 2024; Received in revised form 1 December 2024; Accepted 25 December 2024
Available online 29 December 2024

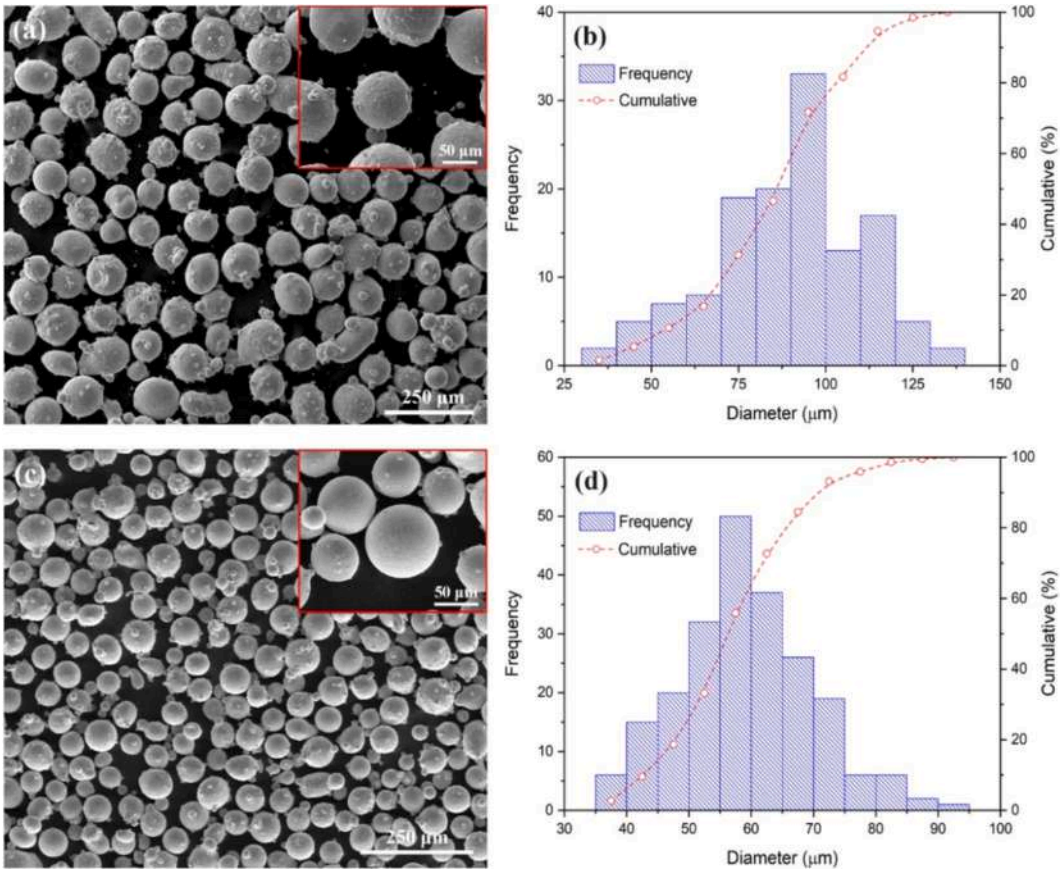

Fig. 1. Morphology and particle size distribution of powder: a, b) AISI 316 L and c, d) IN718.

Table 1
Chemical composition of used AISI 316 L and IN718 powders (wt%).

Element	Fe	Ni	Cr	Mn	Si	Mo	Nb	Ti	Al
AISI 316 L	Bal.	11.7	18.1	1.7	0.6	2.47	–	–	–
IN718	17.7	Bal.	19.5	–	–	3.2	5	1	0.5

steel-nickel based superalloy, which is widely used in critical energy industries, such as power plants and oil refineries, with a favorable balance of economic aspects and functional properties [11,12]. This method of manufacturing the structure is proposed as an alternative solution in the face of its dissimilar welding issues, such as cracking, local corrosion, and residual stress, as regards providing a gradual transition instead of a sharp interface feasibly throughout a part can lead to higher efficiency and longevity [13–15]. So far, several researches have addressed the aspects of processing, microstructure, and mechanical properties of the FGM with a variety in the grade of base alloys and AM techniques. Zhang et al. [16] and Tong et al. [17] studied stainless steel 316 L (AISI 316 L)-Inconel 625 (IN625) FGM produced by L-DED and both observed that the yield strength of the FGM is close to IN625 and its tensile strength is close to AISI 316 L. In a similar work, Chen et al. [18] showed that the wear resistance of FGM is significantly improved when the content of IN625 reaches 60–80 %. Su et al. [19] and Melzer et al. [20] investigated the tensile properties of AISI 316 L-IN718 FGM as-built by L-DED. Further, other works demonstrated that microstructural evolution including the precipitation of secondary phases (especially at higher IN718 content) through post-heat treatment leads to the improvement of mechanical properties [21,22] and hot corrosion resistance [23] of the FGM. In addition, EB-PBF [24] and L-PBF [25,26] processes were successfully used to produce AISI 316 L-IN718 bimetallic structure. Furthermore, Wen et al. [27] realized a compositionally graded alloy (CGA) perpendicular to the build direction via L-PBF and reported that the heat treatment of double aging leads to the loss of yield strength and tensile strength of AISI 316 L-rich sections and brittleness of IN718-rich sections. Also, some researchers investigated wire arc additive manufacturing (WAAM) of AISI 904 L-Hastelloy C-276 [28], AISI 316 L-IN825 [29], and AISI 316 L-IN625 [30] structures and unanimously showed that the inherent high dilution of the process leads to gradient interfaces and strong metallurgical bonding between the layers.

Despite the progress made and overall promising results in the above review, some credible studies reported susceptibility to cracking defects in the AM of stainless steel-nickel based superalloy structures. This concern is more or less present in all 3 AM processes of L-DED [31–35], L-PBF [36–38], and WAAM [39] for various alloy grades. In the case of AISI 316 L-IN718 FGM combining good mechanical properties and corrosion resistance applicable for the elevated-temperature and harsh service environment such in power plants, Kim et al. [33] found the compositional range of 20–30 wt% IN718 to be defective when fabricated by L-DED, while Yang et al. [34] observed crack formation at different positions of non-graded and graded samples. Nevertheless, both of them explained ceramic oxides, precipitation, and columnar-to-equiaxial transition (CET) as factors of the crack initiation and propagation. Meanwhile, other researchers found the bimetallic interface prone to cracking due to the mismatch between energy and material [35–37]. Hence, it seems that there is no comprehensive consensus about the susceptibility to FGAM cracking of the AISI 316 L-IN718 structure and its prevention, and further investigation is needed.

Therefore, the present research studies the fabrication of different designs of AISI 316 L-IN718 FGM by L-DED to provide crack formation mechanisms in susceptible compositional regions and to achieve a compatible (crack-free) FGM design for laser additive manufacturing. In

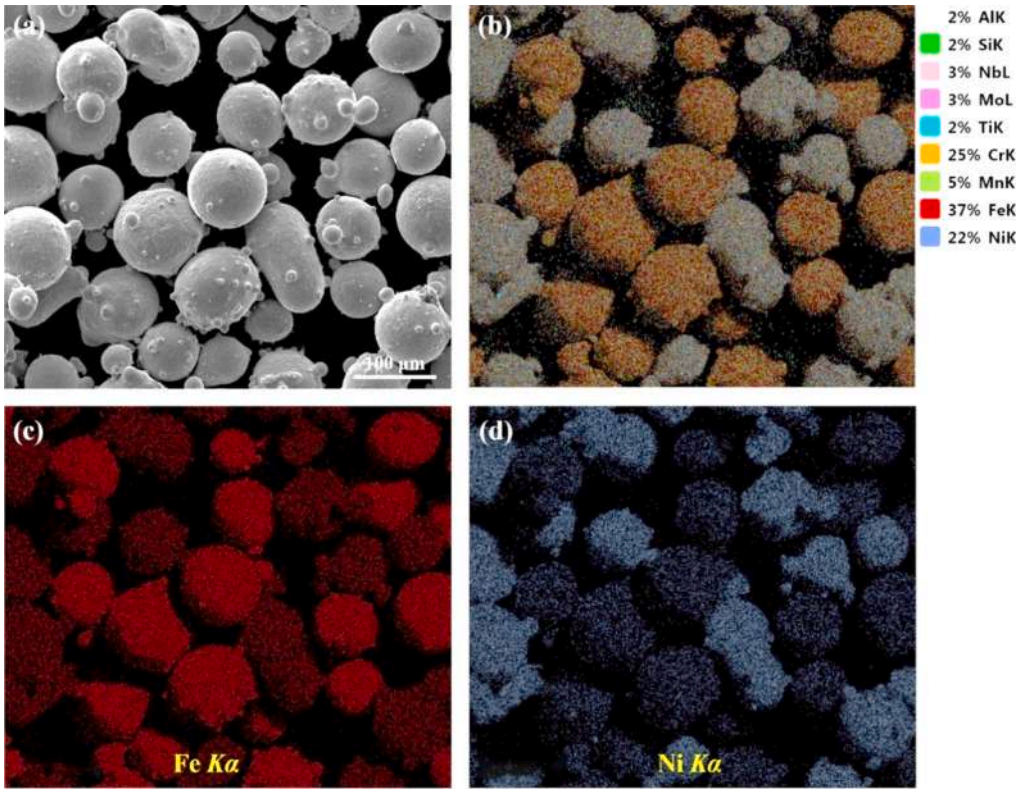

Fig. 2. a) SEM image and b-d) its elemental distribution maps of for a 50:50 weight ratio mixture of AISI 316 L and IN718 powders.

addition, the mechanical properties of the FGMs are evaluated to develop their processing-microstructure-properties relationship.

2. Materials and methods

2.1. FGM design and L-DED process

The feeding materials in the form of gas-atomized powders (supplied by LPW Technology Ltd.) with the morphology and particle size distribution of AISI 316 L ($D_{10} = 53.5$, $D_{50} = 86$, $D_{90} = 111.5$ μm) and IN718 ($D_{10} = 42.5$, $D_{50} = 56$, $D_{90} = 71$ μm) in Fig. 1 and AISI 316 L stainless steel plate with dimensions of 150 × 80 × 8 mm^3 as the building platform were used.

The chemical composition of the alloy powders is presented in Table 1. Also, three weight ratios of 50:50, 75:25, and vice versa were prepared from the primary powders through uniform mechanical mixing in separate containers to fabricate gradient zones with the desired composition.

For example, the powder sampled from the weight ratio of 50:50 and the distribution maps of elements on it are shown in Fig. 2. L-DED additive manufacturing machine equipped with a continuous fiber laser (Convergent Photonics CF1000, Italy) with a maximum power of 1000 W, a wavelength of 1070 nm, and a spot size of 1 mm, a multi-nozzle deposition head (Optomec Inc., USA), carrier and shielding argon (Ar) gas, and rotating disc-type powder feeding system were employed in this research. More information about the L-DED machine is available elsewhere [40].

Based on our previous study on thin-walled FGMs [41], to evaluate the cracking susceptibility of compositional gradient regions and the mechanical behavior of the studied structure, cubic FGM samples were designed and named as shown in Fig. 3. The deposition sequence here was considered starting with AISI 316 L since the inverse one has been demonstrated high cracking susceptibility [31]. For each transition design between base alloys, two cubic samples with different dimensions were considered for microscopy characterizations (Fig. 3a, c, e) and the possibility of preparing tensile test samples (Fig. 3b, d, f). In order to minimize the porosity defect, processing parameters were used according to each region of FGM structures.

For this purpose, in a preliminary study, several cubes of pure AISI 316 L and IN718 alloys were produced through a full factorial design of experiment (DoE) taking into account different levels of key processing parameters (including laser power, scanning speed, powder feeding rate, and hatch distance) and were evaluated for internal defects by Archimedes test and X-ray computed tomography, CT (voltage: 220 kV, current: 190 μA, voxel size: 17 μm, source-to-sample distance: 150 mm, sample-to-detector distance: 1000 mm) methods. More details on the DoE for the processing parameters can be found in the recently published work [40]. Fig. 4 shows the samples of the cubes produced in that evaluation along with the three-dimensional CT images, which indicate the high density of the parts (>99.5 %, noting the detection limit in the voxel size used) and the suitable processing conditions of each one. Thereby, the processing conditions of the pure regions in the FGM structures were obtained and for the gradient zones were also determined according to their nature close to the base alloys, which are presented in Table 2. Fig. 5 shows the cubic FGM structures produced by the L-DED process, indicating almost good dimensional accuracy compared to their design (Fig. 3) though some surface oxidation and adhered powder particles during the process have led to a deviation from the ideal surface quality and dimensional accuracy. It should be noted that the FGM samples designed for the microscopy characterizations were produced in three replicates to ensure the reproducibility of the process.

2.2. Characterization and evaluation

In order to characterize the microstructure, a cross-section was removed from the middle of the FGM samples by wire electrical discharge machining (WEDM), and their surface was prepared by

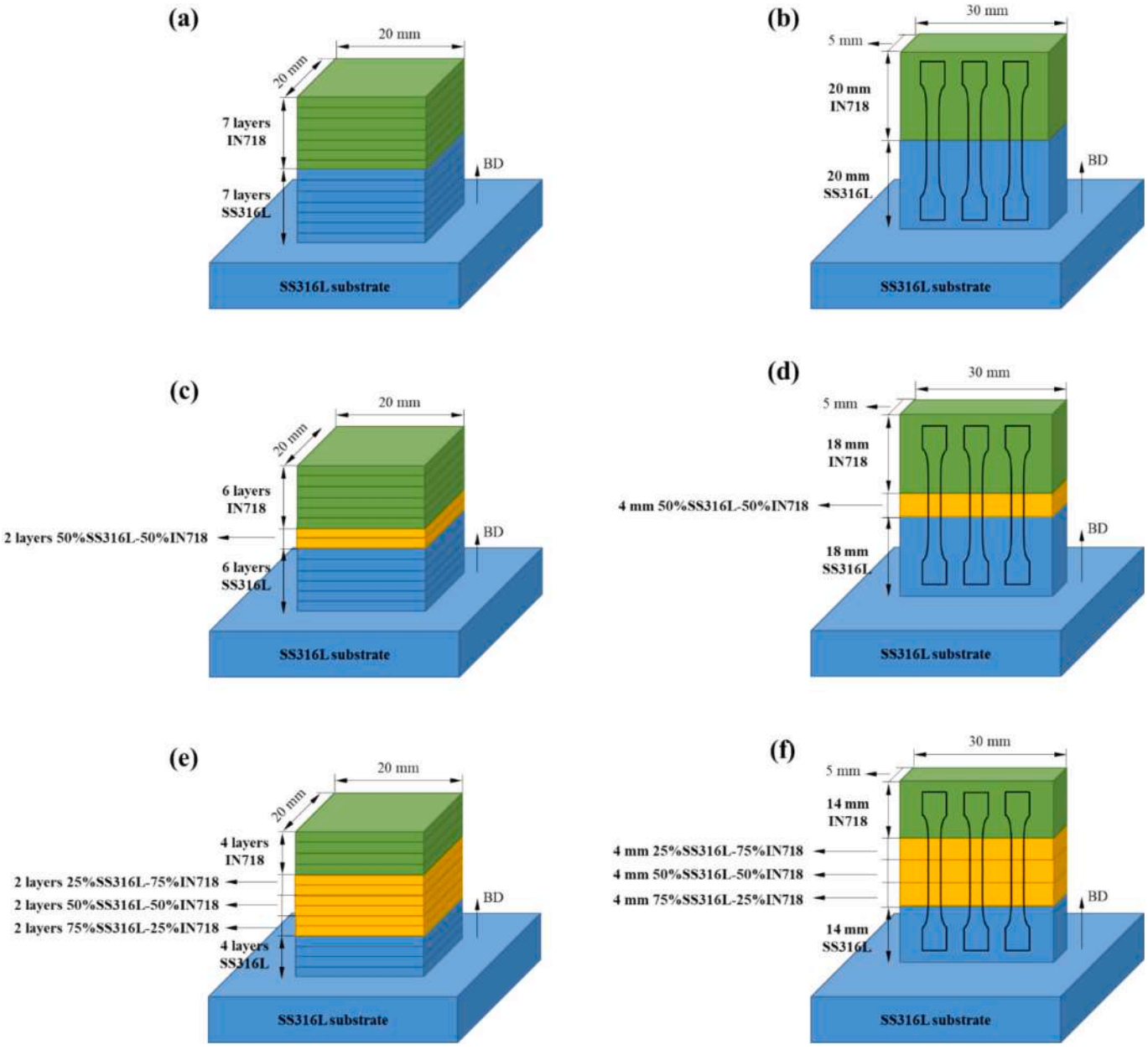

Fig. 3. The design of cubic FGM samples: a, b) multi-material (MM), c, d) FGM-50 % and e, f) FGM-25 %.

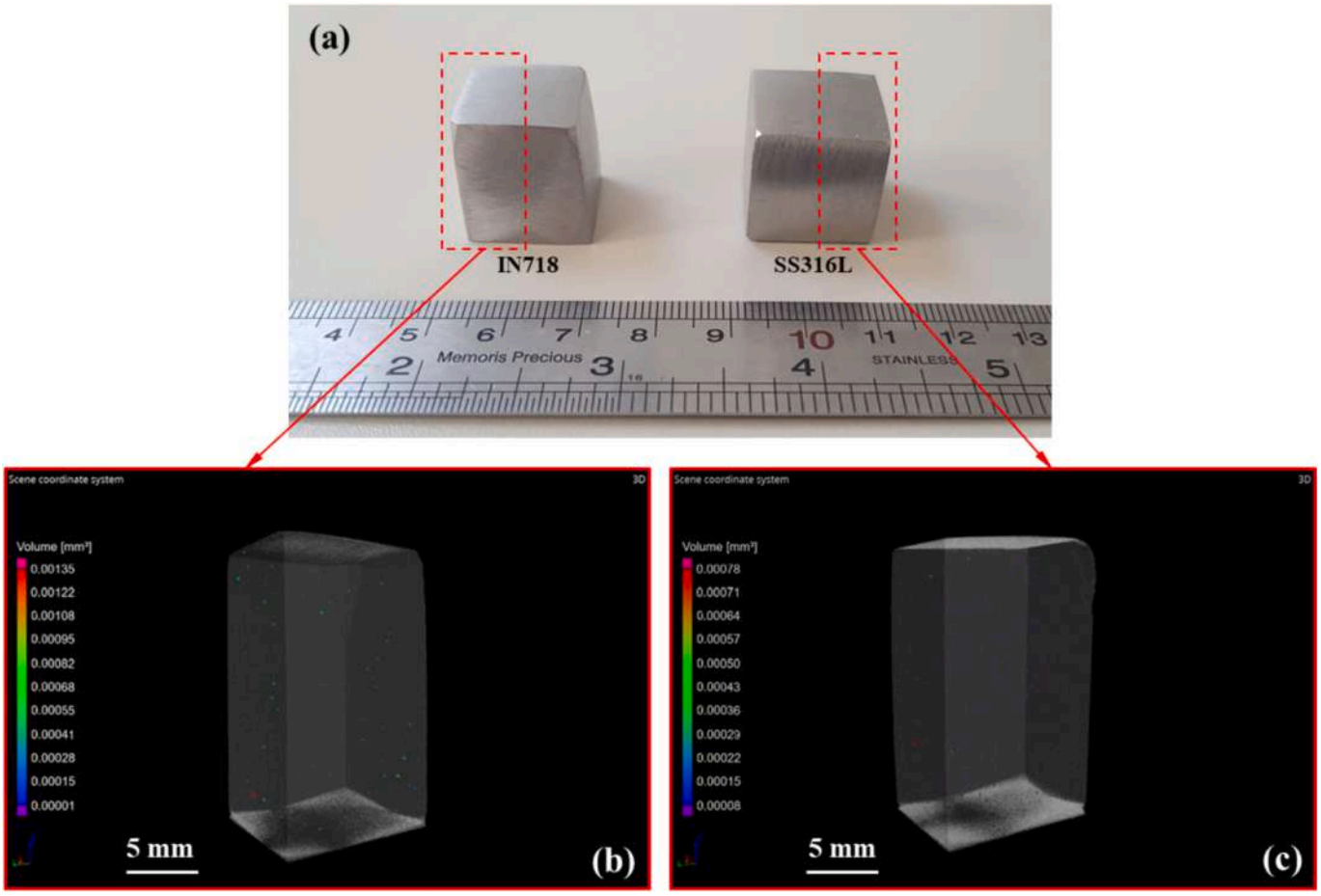

Fig. 4. The preliminary evaluation to achieve processing conditions with minimal internal defects (esp. porosity): a) cubes produced from pure AISI 316 L and IN718 alloys, b, c) three-dimensional CT images of half of the cubes in (a) showing the volume fraction of porosity in each.

standard metallographic methods. Then the surfaces were etched in 15 mL HCl + 5 mL HNO_3 solution for 10 s and evaluated by optical microscopy (Olympus, Japan) and scanning electron microscopy (FEI ESEM QUANTA 200, USA). An X-ray energy diffraction spectroscope (EDAX EDS Silicon Drift 2017, USA) operated in the scanning electron microscope was used to semi-quantitatively analyze the distribution of constituent elements and the chemical composition of possible phases in the microstructure. Moreover, additional surface preparation, including automatic polishing in 3 and 1 μm diamond suspension and electrochemical polishing with 6 vol% HClO4 + 94 vol% CH_3COOH solution at 50 V for 10 s, was carried out to evaluate the evolution of the crystallographic texture, grain structure, grain boundaries, and crystal defects in the FGM samples by electron backscattered diffraction (EBSD) analysis inside a field emission scanning electron microscope (FE-SEM Zeiss Sigma 500 VP, Germany). For each sample, EBSD was performed in two windows of 1.75 × 1 mm^2 in the build direction from the interface of the FGM regions with the conditions of 6 μm step size, 25 kV accelerating voltage, 10 nA probe current, 12 mm working distance, and 70° sample tilt angle and the results were analyzed by HKL-Channel 5 software. To appraise the mechanical properties and behavior, a uniaxial tensile test (Instron 5500R, UK) with a crosshead rate of 2 mm/min and a gauge length of 20 mm was implemented on the samples prepared according to Ref. [19] shown in Fig. 6 by WEDM from the FGMs built for this purpose. Then, tensile properties including yield strength (YS), ultimate tensile strength (UTS), percent elongation (EL), and toughness (integrating the area under the stress-strain curve) were derived from the stress-strain curves and reported as mean values ± standard deviation (STD). Additionally, the fracture surfaces were evaluated by SEM.

3. Results and discussion

Fig. 7a shows numerous cracks in the macrostructure of the 75 % AISI 316 L-25 % IN718 region of FGM-25 %, which indicates the high susceptibility of this region to cracking and was also observed in previous studies [34]. The jagged and uneven edge of the crack morphology in Fig. 7b reveals that its formation occurred as a hot crack. As demonstrated in our recent study [42] through finite element (FE)

Table 2
Process parameters used to produce cubic FGM structures.

Parameter	Value	
Power (W)	400	
Scanning speed (mm/min)	750	
Powder feeding rate (g/min)	6	
Air blow (L/min)	15	
Carrier gas flow (L/min)	6	
Shielding gas flow (L/min)	10	
Standoff distance (mm)	10.5	
Scanning strategy	0°/90° (raster)	
Compositional region	Hatch space (mm)	*Z*-step (mm)
100 % AISI 316 L	0.414	0.271
75 % AISI 316 L + 25 % IN718	0.414	0.271
50 % AISI 316 L + 50 % IN718*	0.404	0.332
25 % AISI 316 L + 75 % IN718	0.404	0.332
100 % IN718	0.404	0.332

* In the experimental evaluations of the production of this compositional region with the processing parameters of pure IN718 compared to pure AISI 316 L, fewer internal defects were observed.

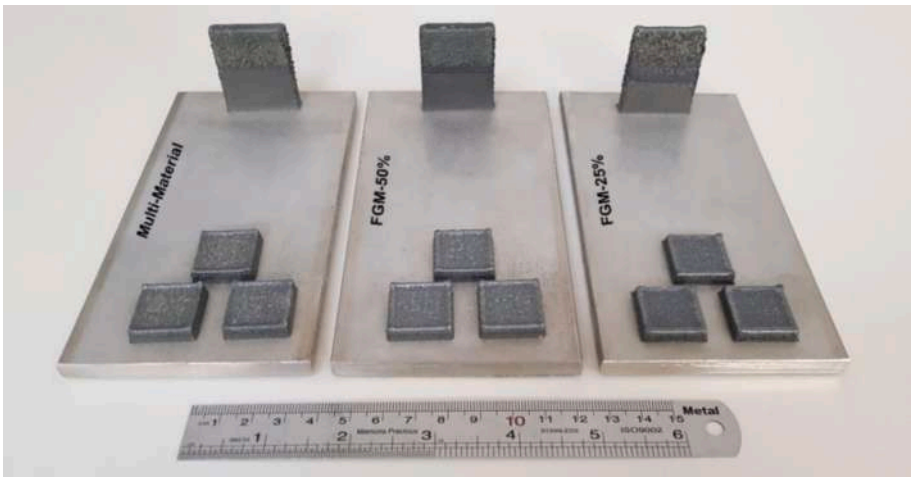

Fig. 5. The cubic FGM structures produced as designed in Fig. 3 by L-DED.

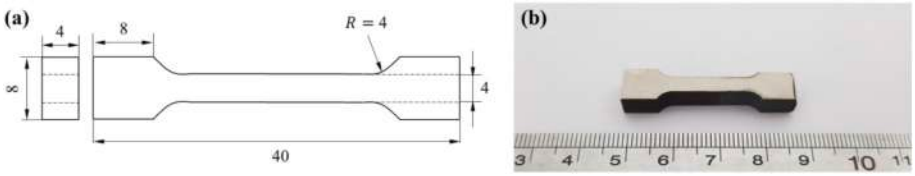

Fig. 6. a) Geometry (mm) and b) image of tensile sample.

modeling, the design of FGM-25 %, similar to FGM-50 % from a mechanical point of view can effectively resolve the issue of concentration and sharp change of residual stresses at the interface of the multi-material structure between the base alloys, as shown in Fig. 8, owing to the reduction in properties difference of adjacent compositional regions. However, here from a metallurgical perspective, the structure of FGM-25 % is highly susceptible to hot cracking in the remarked region, which could adversely affect its properties and performance.

In spite of some black dots in Fig. 7e indicating oxide inclusions (Si/Mn-rich) from the powder feedstock [43], it can be seen that the solidification structure in the build direction (Fig. 7e-c) has evolved from columnar cell morphology to columnar dendritic to equiaxed dendritic morphology due to the increased undercooling and has become coarser as the cooling rate decreases due to the heat accumulation [44,45]. In order to find out the metallurgical origin and understand the mechanisms of crack formation in the FGM-25 % structure, more details were studied by different techniques, which will be discussed below.

Fig. 9 shows the SEM micrographs of the crack and its marked areas. The different contrast along the crack origin (Fig. 9a, c) is evidence of the formation of a continuous liquid film, which can be caused by the low melting point compounds exposed to the deposition heat of the upper layer. In addition, the different directions of growth and development of the microstructure around the crack origin (Fig. 9c) elucidate that the liquid film was formed at the boundary of two adjacent grains, which justifies its continuity. In such conditions and under the thermal stresses caused by the solidification shrinkage and solid-state contractions during the process, it is expectable that the crack nucleation has occurred inter-granularly. Nevertheless, further evaluation of the crack length indicates that in addition to the inter-granular mode, its propagation also occurred intra-granularly (through solidification sub-grain boundaries, SSGBs) as illustrated in Fig. 9b, d related to the middle of the crack length.

In order to determine the chemical composition and identify possible phases around the crack, semi-quantitative EDS analysis was used on the numbered locations in Fig. 9c, the results of which are shown in Fig. 10. From the core of the dendrite adjacent to the crack (location #1) to the edges (locations #2 and #3) and especially its origin (location #4), microsegregation of Nb and Mo elements with a low partition coefficient can be discerned.

Although it cannot be certain about the content of the light carbon element, as a rough estimate similar to Ref. [14] the analysis of location #3 indicates the formation of segregated metal carbides and further the formation of Laves intermetallic phase (analysis of location #4) through the eutectic reactions of $L \rightarrow \gamma + MC$ and $L \rightarrow \gamma +$ Laves, respectively. The formation of such low melting compounds at the origin and edge of the crack, besides the previous evidence, well confirms the occurrence of the liquation crack, which has been declared in related studies [32,39]. Furthermore, the detection of oxygen in location #3 can indicate the presence of oxide compounds arising from the used powder or oxidation during the process, which according to proven findings [33] would lead to discontinuity and deterioration of cracking in the structure. In the following, further evidence of the traces of unwanted oxide compounds will be presented and discussed. However, it seems that another important factor plays a role in the cracking susceptibility of the FGM-25 % structure, because obviously and also according to thermodynamic calculations in [33] the fraction of carbide and intermetallic phases (the source of grain boundary liquid film through the reversal of the low-temperature eutectic reactions) increases with greater participation of IN718. While no trace of cracking was found in IN718-rich regions of FGM-25 % structure.

Fig. 11 shows the results of the EBSD analysis of the multi-material (MM) structure from the two interfaces of AISI 316 L/IN718 and the structure/substrate in the build direction. The white dashed line in the inverse pole figures (IPFs, Fig. 11a, b) determines the position of the interface on each of them, which for the interface in Fig. 11a, the distribution maps of Ni and Fe elements (Fig. 11c, d respectively) support the accuracy of its position. In the IPF maps, at the beginning of the deposition of each region due to the high-temperature gradient, especially at the structure/substrate interface (Fig. 11b), a finer grain structure is observed and further, due to the heat accumulation and the reduction of the temperature gradient, coarser grains have been formed through the competitive growth mechanism in line with the maximum

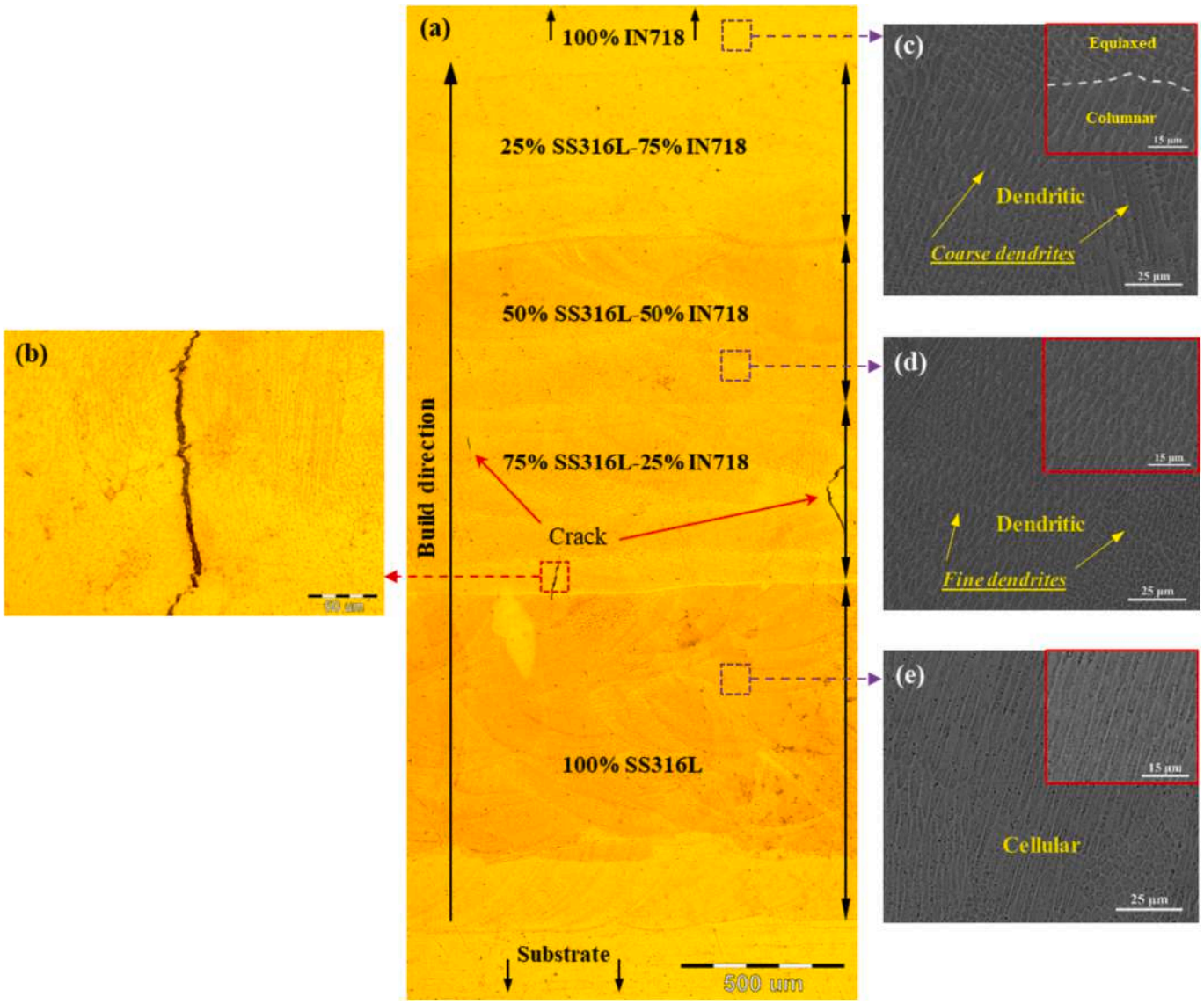

Fig. 7. a) Cross-sectional macrostructure of FGM-25 % sample and b) crack surrounding in a high magnification of the area marked in (a), c,d,e) Microstructure of 100 % AISI 316 L, 50 %–50 %, and 100 % IN718 regions, respectively.

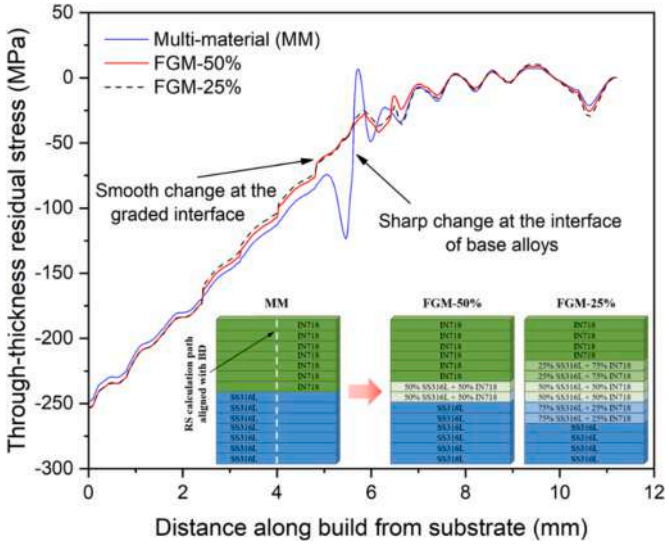

Fig. 8. Variations of through-thickness residual stress (RS) along building direction (BD) on the thin-wall MM (blue line), FGM-50 % (red line), and FGM-25 % (black dashed-line) structures displayed at the bottom of the diagram [42]. (For interpretation of the references to colour in this figure legend, the reader is referred to the web version of this article.)

temperature gradient. The predominance of this mechanism and its being affected by the successive change in the scanning direction (SD) has prevented the growth of grains in a certain direction. In addition, in the interface of AISI 316 L/IN718, the sharp difference in the chemical composition has disturbed the epitaxial growth to some extent and has aggravated the situation. The distribution of high and low angle grain boundaries in the build direction in Fig. 11f, h, in addition to clarifying the misorientation angle histogram (Fig. 11e) as a transition from the worked structure of the substrate with a mass of high-angle boundaries to the MM solidification structure with multiple sub-grain (low-angle) boundaries, confirms the above findings on the competitive growth in another way. Besides, the distribution maps of the kernel average misorientation (KAM) in Fig. 11g, i show two accumulations of crystal defects near the interfaces (areas bounded by dashed lines), which are qualitatively reminiscent of local strain and residual stress concentration. In other words, the major temperature gradient at the structure/substrate interface (Fig. 11i) has led to the evolution of high local strain and stresses, resulting in a relatively large accumulation of dislocations and solidification sub-boundaries. While at the AISI 316 L/IN718 interface (Fig. 11g), despite the formation of a dilution zone (DZ) in a width of about 200 μm (Fig. 11c, d), the accumulation of defects (though with a shorter range) can be observed due to the difference in the thermo-physical properties of the base alloys and local strain.

Fig. 12 shows the results of the EBSD analysis of the FGM-50 % structure from the interface area of AISI 316 L/50–50/IN718 and the structure/substrate in the build direction. In addition to the evolution of the grain structure similar to the previous case, the detection of micro-inclusions in the 50 %–50 % region (Fig. 12d) is another evidence of the role of oxide compounds (induced by powder materials or oxidation) in the process, whose presence causes different phenomena. First, as can be seen from Fig. 12c, d, the presence of oxide has disrupted the melt fluid flow caused by Marangoni convection. This effect, which has been numerically and experimentally demonstrated by Zuback et al. [46], has led to changes in the melt pool shape and the formation of an unmixed zone (UZ). Second, according to Fig. 12f, it has acted as a nucleation site, and thus numerous fine grains have formed around it. On the other hand, although the KAM maps in Fig. 12g, i show the accumulation of crystal defects at the structure/substrate interface (as in the MM structure), at the same time, indicate the lack of defects concentration at the AISI 316 L/50–50/IN718 interfaces due to the properties approximation of the adjacent regions and the reduction of the strain inconsistency compared to the MM structure. However, within the 50 %–50 % region, a concentration of defects around the oxide (Fig. 12g) is observed due to the strain inconsistency. The set of listed consequences caused by the presence of oxide can affect the cracking susceptibility of the studied structures.

Fig. 13 reveals another important fact of the FGM-25 % structure (susceptible to cracking) different from the EBSD analysis results of other structures. The IPF maps in Fig. 13a, b are from the interfaces of 75–25/50–50/25–75/IN718 and 75–25/AISI 316 L/substrate, respectively, which are practically impossible to discriminate except by matching the elemental distribution maps (as in Fig. 13c, d), indicate the development of a preferred texture parallel to the build direction, especially in the initial regions of FGM-25 % (Fig. 13b). Also, from the KAM maps in Fig. 13g, i can be found that although the problem of strain/stress concentration and as a result the high accumulation of defects at the interfaces has been effectively resolved (excluding the substrate vicinity caused by the extreme temperature gradient) due to the proximity of the nature and properties of the adjacent gradient regions, the presence of a microcrack with an accumulation of defects at its two ends (Fig. 13i) and in line with the growth direction of the columnar grains can be seen.

This different evolution of the grain structure, which can facilitate the cracking of the FGM-25 % structure by supporting the continuity of the grain boundary liquid film (how to form was discussed earlier), can be well understood from the pole figures (PFs) of the studied samples (Fig. 14). As can be seen from the comparison of Fig. 14a, c, e related to the window (b) respectively in Figs. 11, 12, and 13 (about the lower half of the structures), for FGM-25 % a much stronger texture (Max. 13.76) has been formed in the {100} plane and a slight deviation from the ⟨100⟩ build direction, which can be due to the reasons of maintaining the temperature gradient caused by pausing and resuming the process when changing the composition of the feeding powder as well as improving the epitaxial growth with closer proximity of the chemical composition and the nature of the adjacent regions. In the following, although the intensity of orientation decreases due to the heat accumulation (reduction of temperature gradient) and the increase in total entropy with the greater participation of IN718 [21,47] in the upper half of the structures (Fig. 14b, d, f), still a preferred orientation (Max. 8.68) is observed for the FGM-25 % structure (Fig. 14f), especially in the {111} plane. Fig. 15

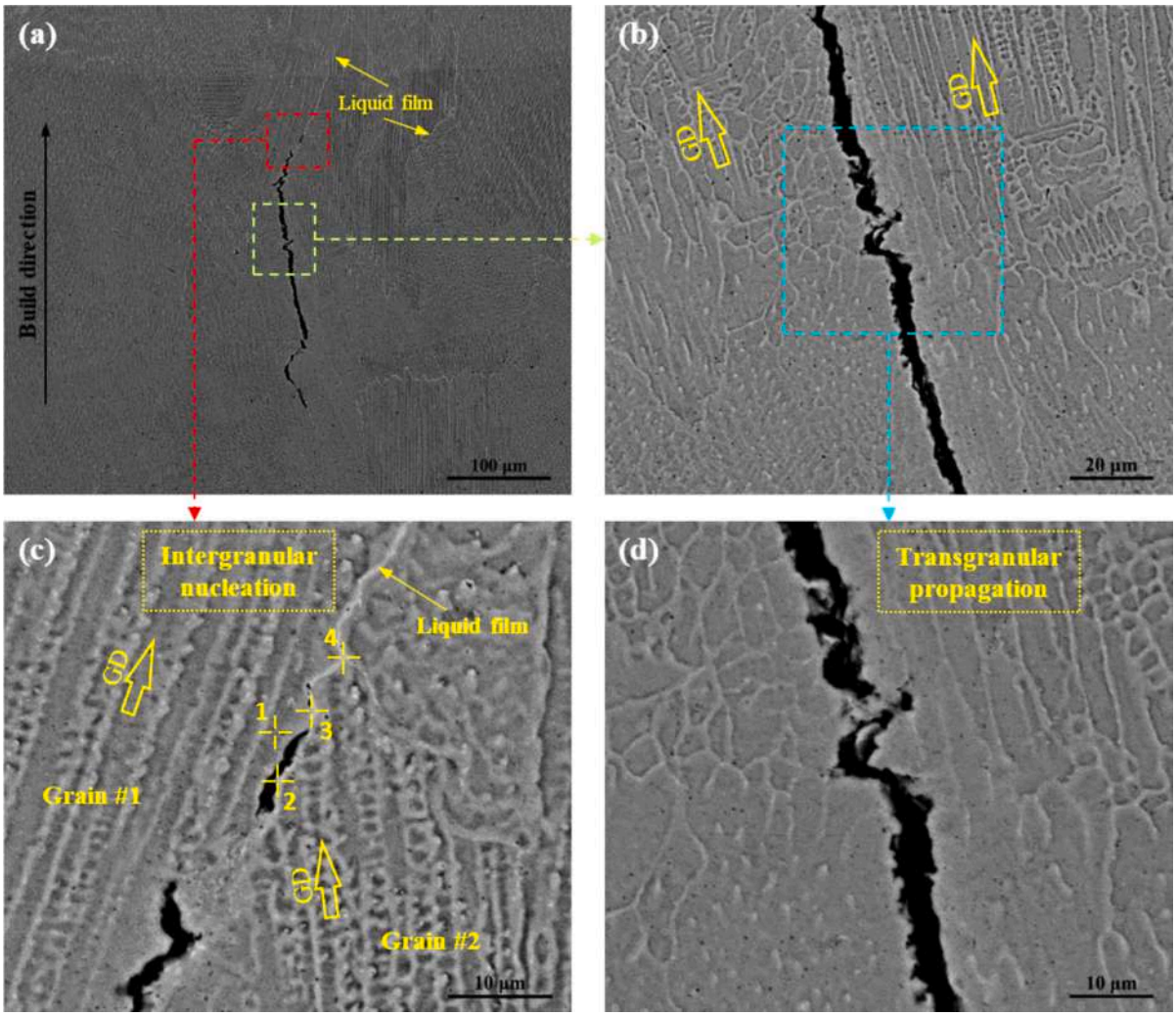

Fig. 9. SEM micrographs: a) morphology of the crack and its surrounding area, b-d) higher magnification of the indicated areas of the crack. The numbered markers in (c) show selected locations for the EDS chemical analysis.

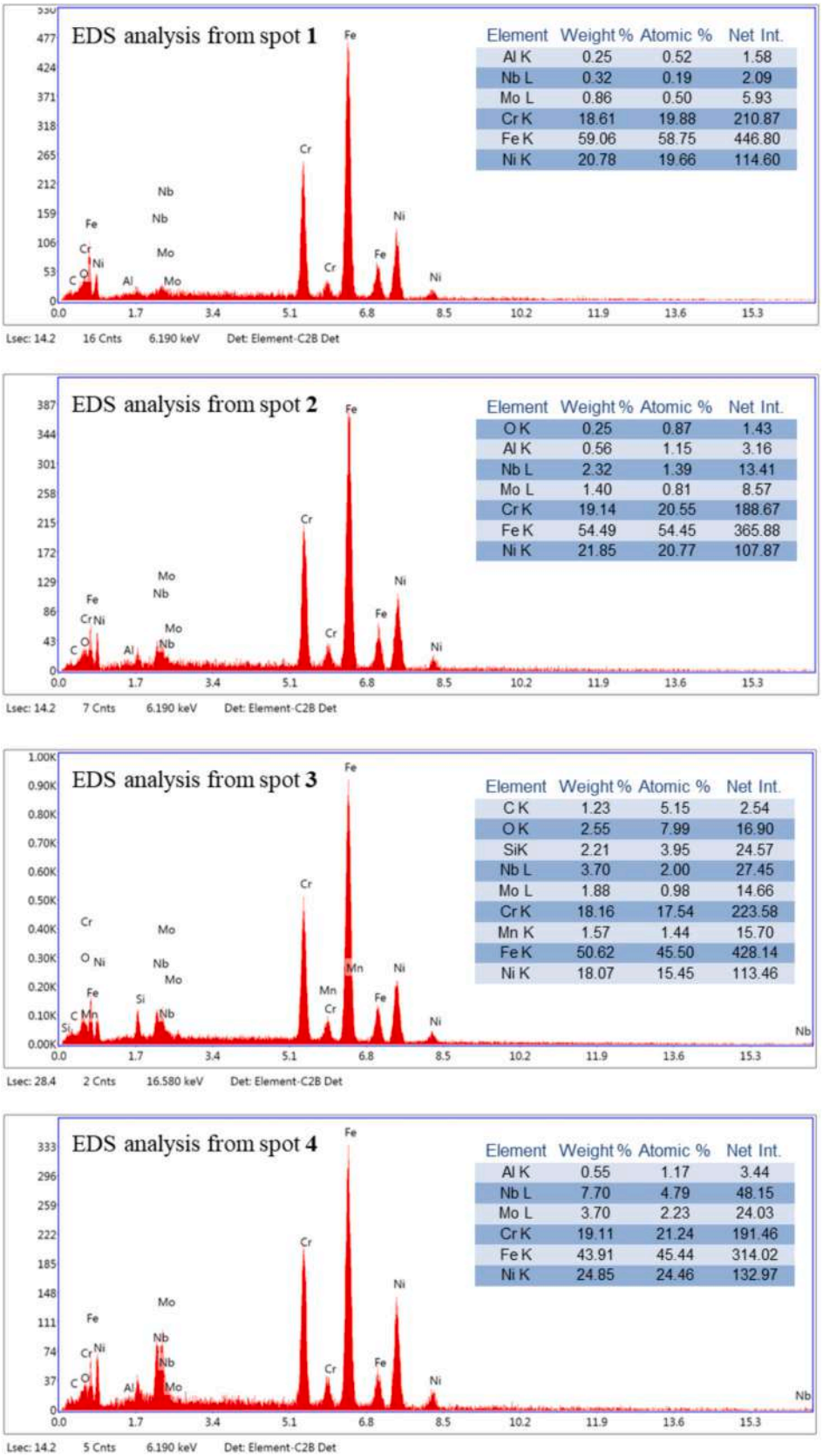

Fig. 10. The results of EDS chemical analysis from the numbered locations adjacent to the crack in Fig. 9c.

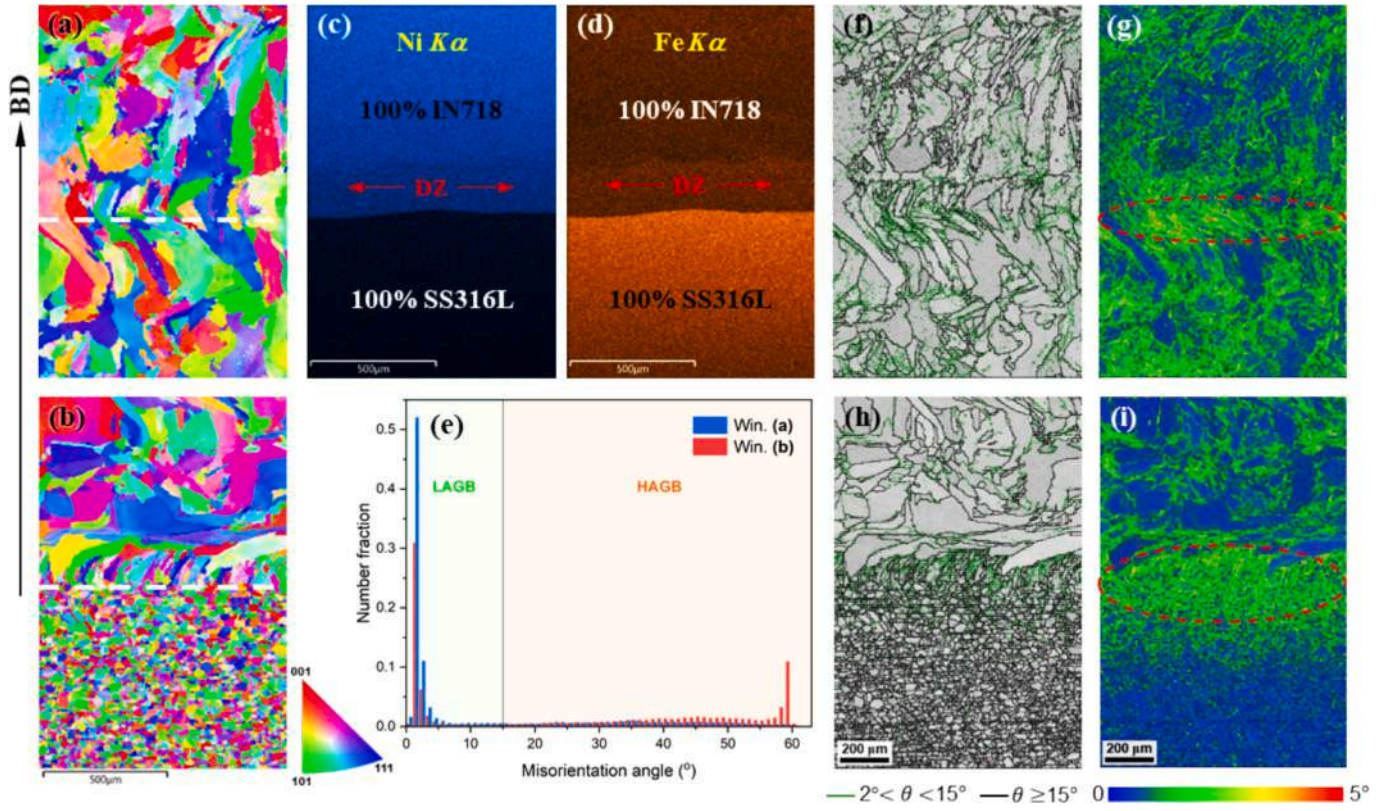

Fig. 11. EBSD analysis results of the MM structure: a, b) IPF X maps from the interfaces of AISI 316 L/IN718 and structure/substrate, respectively, c, d) elemental distribution maps of Ni and Fe, respectively, corresponding to window (a), e) variations of grain boundary misorientation angle in windows (a) and (b), f, g) distribution maps of grain boundary and KAM corresponding to window (a), and h, i) distribution maps of grain boundary and KAM corresponding to window (b). The areas surrounded by red dashed lines in (g, i) show the concentration of crystal defects at the interfaces. (For interpretation of the references to colour in this figure legend, the reader is referred to the web version of this article.)

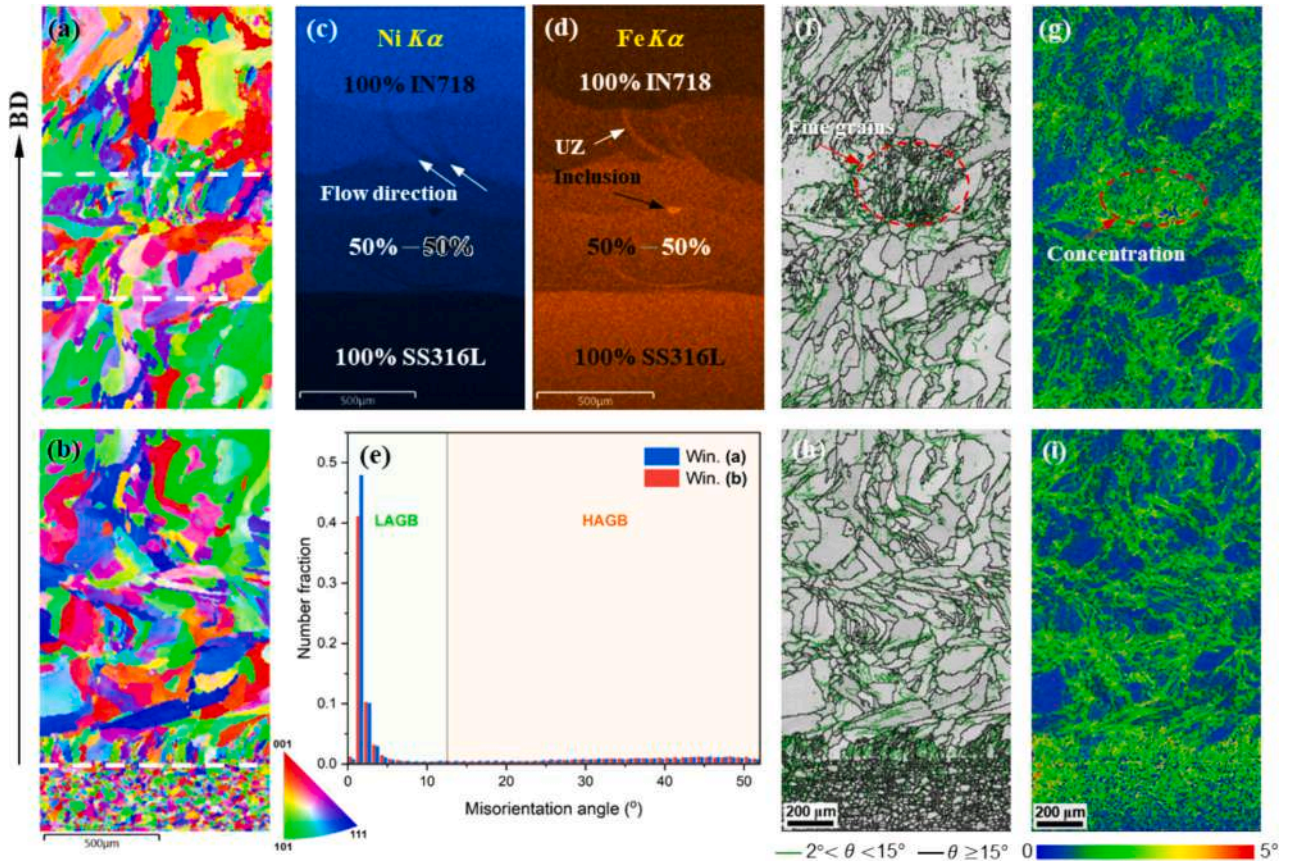

Fig. 12. EBSD analysis results of the FGM-50 % structure: a, b) IPF X maps from the interfaces of AISI 316 L/50–50/IN718 and structure/substrate, respectively, c, d) elemental distribution maps of Ni and Fe corresponding to (a), e) variations of grain boundary misorientation angle in windows (a) and (b), f, g) distribution maps of grain boundary and KAM corresponding to (a), and h, i) distribution maps grain boundary and KAM corresponding to (b).

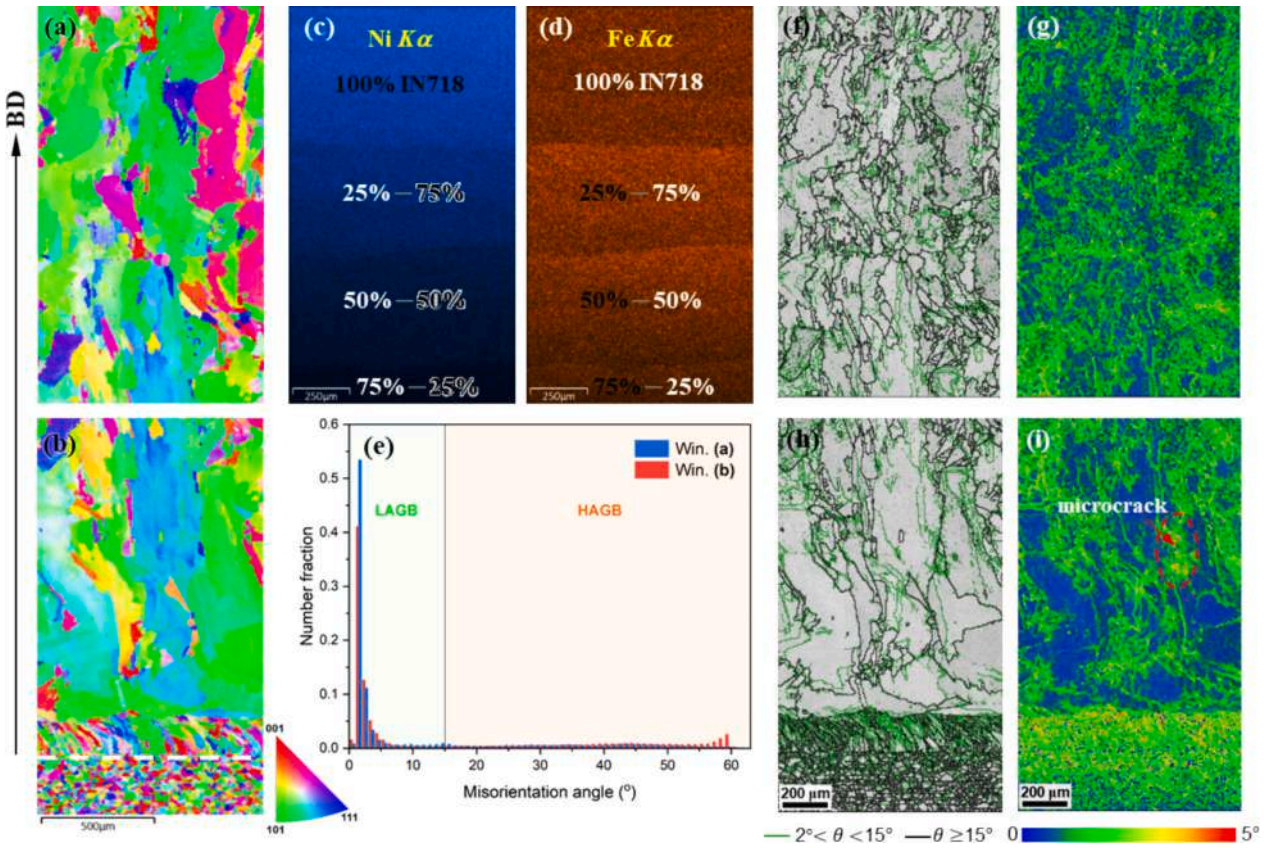

Fig. 13. EBSD analysis results of the FGM-25 % structure: a, b) IPF X maps from the interfaces of 75–25/50–50/25–75/IN718 and 75–25/AISI 316 L/substrate, respectively, c, d) elemental distribution maps of Ni and Fe corresponding to (a), e) variations of grain boundary misorientation angle in windows (a) and (b), f, g) distribution maps of grain boundary and KAM corresponding to (a), and h, i) distribution maps grain boundary and KAM corresponding to (b).

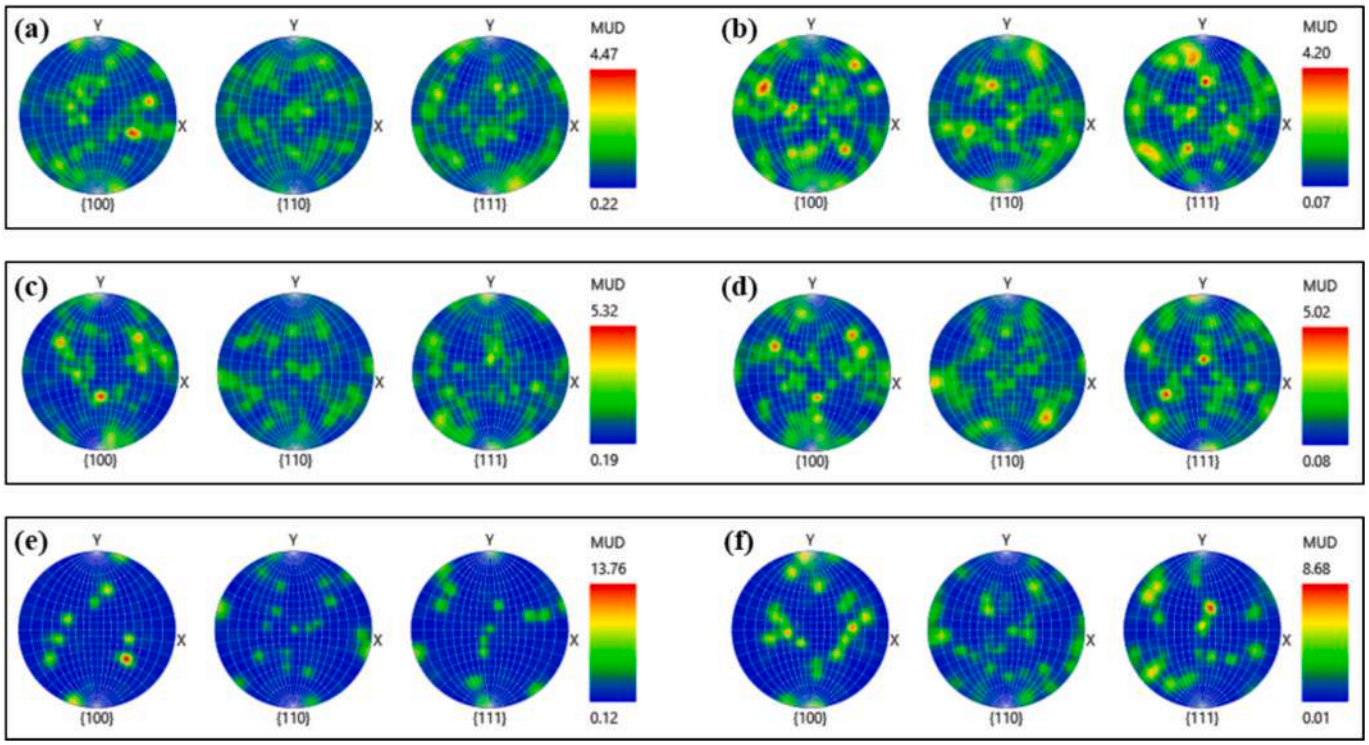

Fig. 14. Polar figures (PFs) of {100}, {110}, and {111} planes related to the structures: a, b) MM, c, d) FGM-50 %, and e, f) FGM-25 %. The left column (a, c, e) and the right column (b, d, f) were obtained from the windows (b) and (a) in Figs. 11, 12, and 13, respectively, in the build direction.

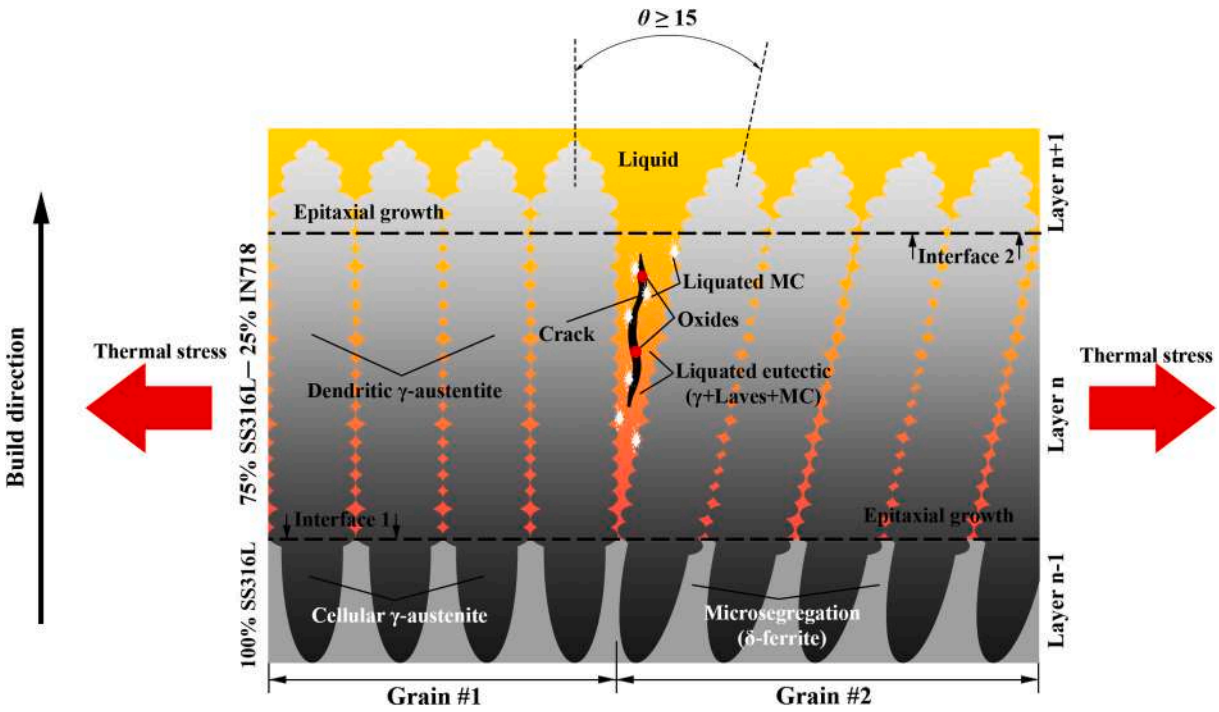

Fig. 15. Schematic of the liquation crack formation mechanism in the susceptible compositional region of 75 % AISI 316 L-25 % IN718 in the FGM-25 % structure.

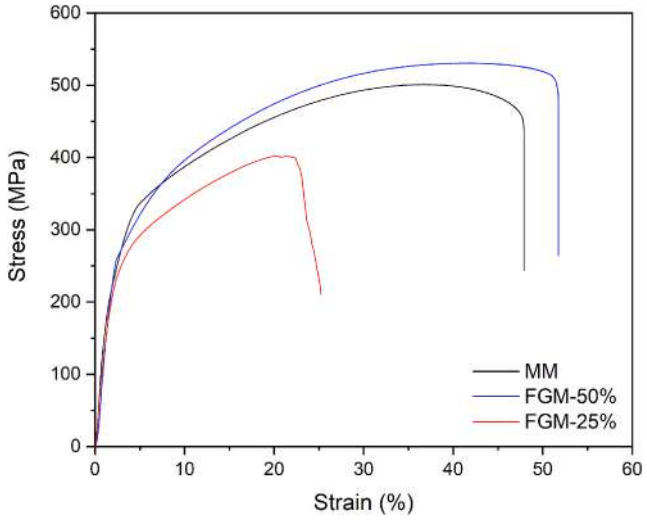

Fig. 16. Engineering stress-strain diagram of uniaxial tensile test of MM and FGM structures.

schematically depicts the role of the directional evolution of FGM-25 % grain structure (*eps.* in its initial regions) in the liquation cracking mechanism of the 75 % AISI 316 L-25 % IN718 susceptible region by providing the conditions for the continuity of the grain boundary liquid film.

Fig. 16 shows the tensile test results in the form of engineering stress-strain curves. As expected, the FGM-25 % structure, which suffers from cracking in the compositional region of 75 % AISI 316 L-25 % IN718, has endured the lowest stress and strain under axial loading, consistent with the results reported in the studies [27,48]. However, the strength drop is less remarkable than the ductility decrease, which can be attributed to the alignment of the loading direction and most cracks length leading to no significant reduction in the load-bearing area. Comparing the stress-strain curves of MM and FGM-50 % structures shows that the tensile properties of both are close to pure AISI 316 L (mean tensile strength ≈ 600 MPa, mean elongation ≈ 55 %) but more ductile than pure IN718 (mean tensile strength ≈ 950 MPa, mean elongation ≈ 35 %) reported elsewhere [34], while the latter design is somewhat superior. However, to make a better judgment, the quantities obtained from the tensile test for each structure were summarized in the charts of Fig. 17. Even though the FGM-50 % structure determines the best mechanical properties by recording the maximum tensile strength, elongation, and toughness up to 540 ± 10 MPa, 52 ± 2 %, and 24 ± 1.4 kJ/mm^3, respectively, considering the standard deviation values indicates that there is not much difference between FGM-50 % and MM structures in the static loading. Nevertheless, that difference can be caused by the mitigation of properties difference and high residual stresses at the sharp interface of the MM structure by redesigning it as the FGM-50 %, which was

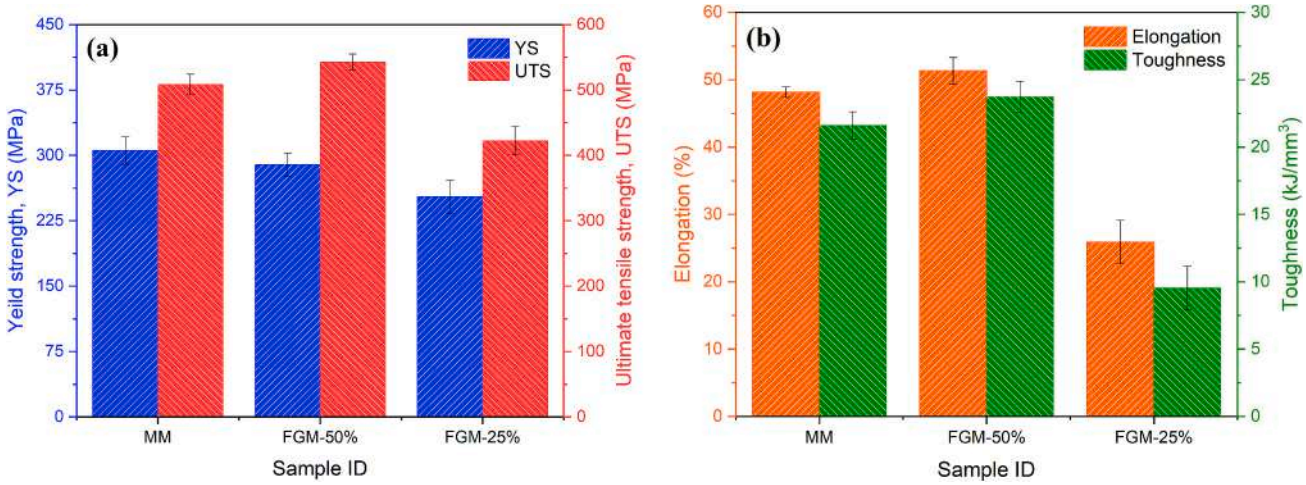

Fig. 17. Comparison of a) yield and tensile strength and b) elongation and toughness of MM and FGM structures.

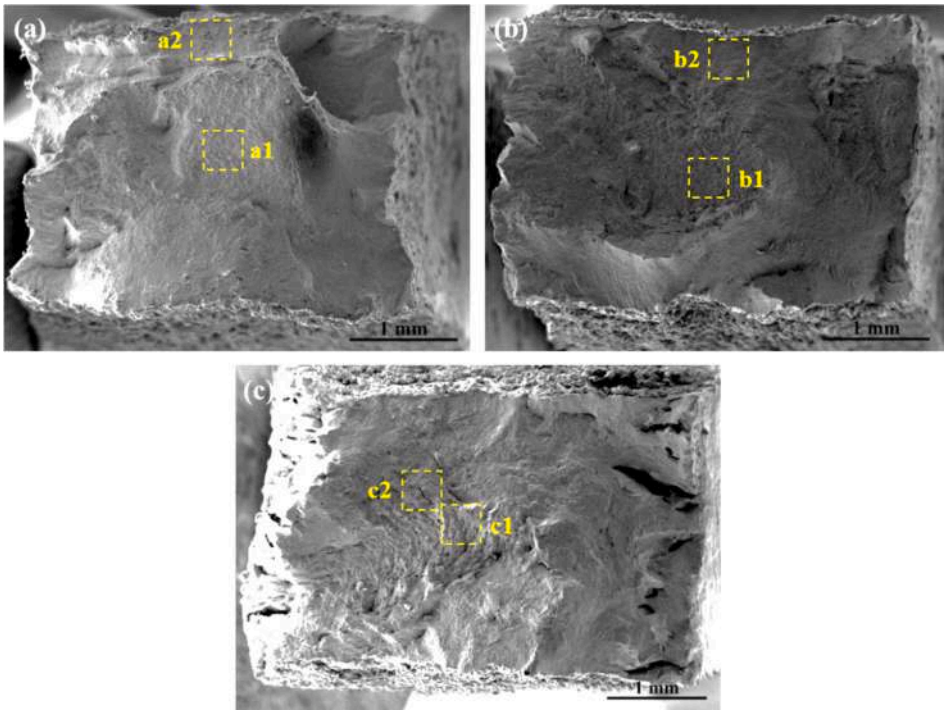

Fig. 18. Macro-scale fractography of the fracture surfaces of structures: a) MM, b) FGM-50 %, and c) FGM-25 %.

numerically and experimentally demonstrated in our previous research [42]. In addition, in terms of performance, Hofmann et al. [5] proved that a car valve stem with a gradient design meets better performance in high-temperature service conditions compared to its dissimilar joint. On the contrary, the FGM-25 % structure with the minimum tensile strength of 420 ± 23 MPa, elongation of 23.5 ± 3 %, and toughness of only 9.5 ± 2 kJ/mm^3 shows significantly the weakest tensile mechanical properties due to high susceptibility to liquation cracking in the compositional region of 75 % AISI 316 L-25 % IN718. Although other sources (e.g., porosity) could be incorporated in such failure, cracks act as localized stress raiser sites with a much smaller radius of curvature (i.e. higher stress concentration factor, k_t) which can much more rapidly propagate than others and disintegrate the FGM structure, thus they are the main cause of failure in the FGM-25 % sample. Therefore, considering the mechanical properties and performance of the studied structures, it is inferred that for the AISI 316 L-IN718 structure, designing a compositional gradient in the form of a 50 wt% mixing region between the base alloys (FGM-50 %) can purposefully lead to its improvement (without both problems of internal stress concentration at the interface of MM and cracking susceptibility in FGM-25 %).

Besides, the structures were subjected to fracture analysis following the tensile test to better understand their mechanical behavior. The fracture position of MM and FGM-50 % structures was similarly determined in the region of 100 % AISI 316 L (weaker base alloy). That is why no significant difference was observed in their mechanical properties. However, the fracture of the FGM-25 % structure occurred from the 75 % AISI 316 L-25 % IN718 region. Fig. 18 shows the macrographs of the fracture surfaces of each structure. The appearance of cup and cone fracture indicates the occurrence of ductile fracture in all three, with the difference that for the FGM-25 % (Fig. 18c) multiple cracks can be observed on the fracture surface.

For more details, SEM micrographs from the areas specified in Fig. 18

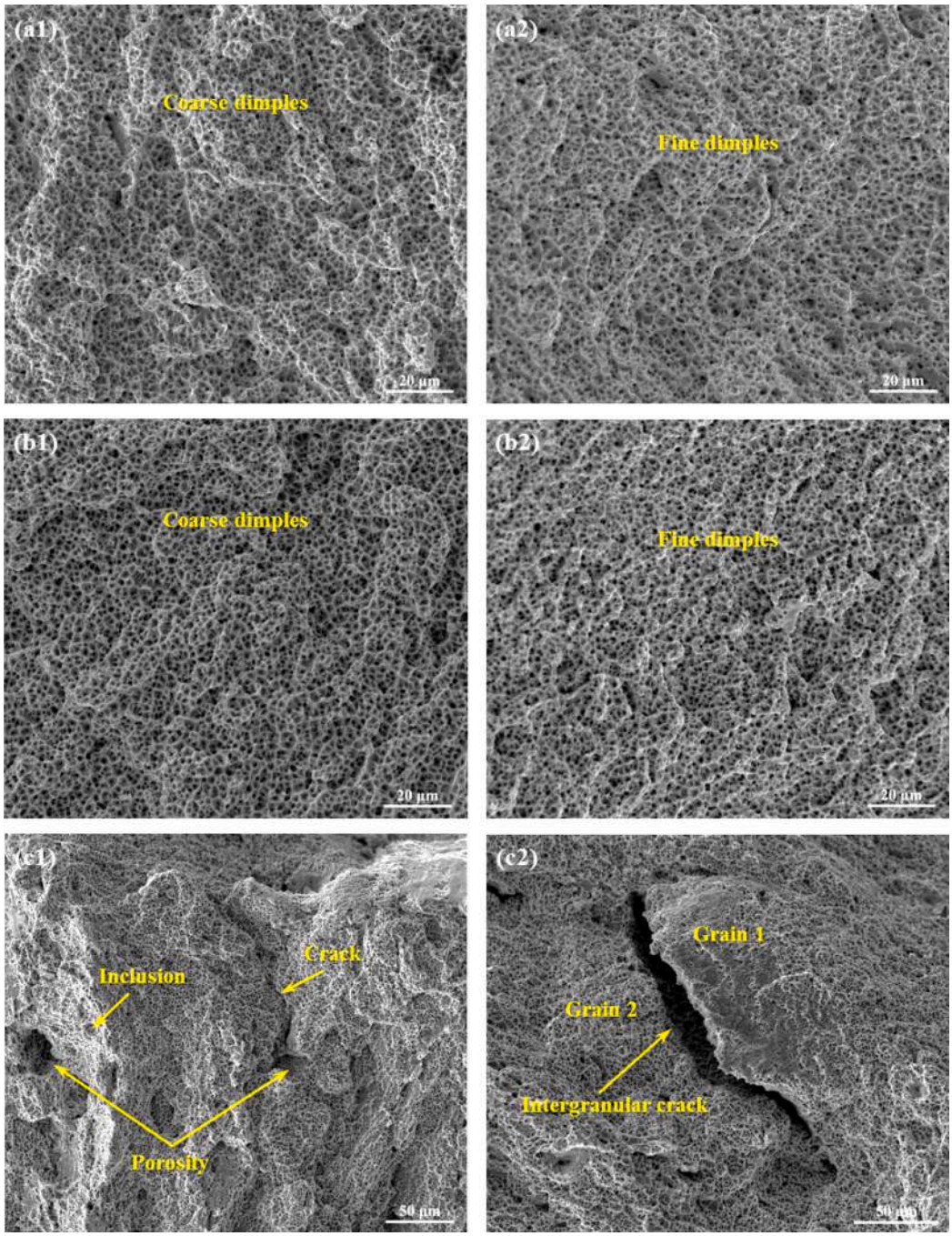

Fig. 19. SEM micrographs of the fracture surfaces from the areas specified in Fig. 18.

for each are presented with higher magnification in Fig. 19. The dimple morphology confirms the ductile fracture of all three structures, with the explanation that the coarser dimples in the center (Fig. 19a1, b1) and the finer dimples at the edge (Fig. 19a2, b2) of the fracture surfaces can be due to the change of plane strain state to plane stress. Meanwhile, the evaluation of the FGM-25 % fracture surface in Fig. 19c1, c2 shows the presence of porosity, oxide inclusion, and especially (intergranular) crack defects related to the 75 % AISI 316 L-25 % IN718 region, which can be interpreted as another evidence of the cause on the loss of tensile properties of this structure. In other words, those defects act as localized stress risers (*esp.*, the crack with the smallest radius of curvature) within the part, confining plastic deformation and decreasing both strength and ductility of the FGM-25 % sample resulted in the premature failure. While, in two other samples (MM and FGM-50 %), the hardening and softening mechanisms compete to the final fracture without any disruption by no significant internal defects.

4. Conclusion

In the present research, the compatible design for the laser additive manufacturing of AISI 316 L-IN718 FGMs by the L-DED method was studied from various metallurgical and mechanical aspects. The main findings are summarized as follows:

1) Even though from a mechanical point of view, the problem of high residual stress concentration at the sharp interface of the multi-material (MM) can be effectively resolved by designing FGM-50 % and FGM-25 % structures, multiple cracks in the compositional

region of 75 % AISI 316 L-25 % IN718 (in cases with a length of more than 100 μm) indicate a serious metallurgical weakness of the FGM-25 % structure and its failure.

2) In determining the mechanism of cracking, the identification of the formation of a grain boundary liquid film through the melting of low-temperature eutectic compounds (γ + Laves+MC) and its continuity caused by the epitaxial growth and preferential orientation of the grain structure in the above-mentioned region, indicates the occurrence of liquation cracks. Also, the proven presence of oxide micro-inclusions and porosities has aggravated the imperfection of the structure and cracking.
3) The evaluation of mechanical properties and behavior in the condition of uniaxial tension showed that the FGM-50 % structure is the best with the maximum tensile strength, elongation, and toughness with values of 540 ± 10 MPa, 52 ± 2 %, and 24 ± 1.4 kJ/mm^3, respectively, though these values are statistically comparable to those of MM in such static loading condition. In contrast, the FGM-25 % gives the weakest results with a fracture from the cracked region.
4) Although the ductile fracture of MM and FGM-50 % structures occurred in the 100 % AISI 316 L region (weaker base alloy) and caused their tensile properties to be close, it is obvious that the effective reduction of the problem of concentration of interfacial residual stresses in the FGM-50 % can lead to improved performance in critical service conditions by the properties proximity of adjacent regions.

CRediT authorship contribution statement

Reza Ghanavati: Conceptualization, Data curation, Formal analysis, Investigation, Methodology, Visualization, Writing – original draft. **Homam Naffakh-Moosavy:** Conceptualization, Methodology, Supervision, Validation, Writing – review & editing. **Mahmoud Moradi:** Data curation, Writing – review & editing. **Federico Mazzucato:** Data curation, Formal analysis, Methodology, Writing – review & editing. **Anna Valente:** Methodology, Validation, Writing – review & editing. **Sara Bagherifard:** Formal analysis, Validation, Writing – review & editing. **Abdollah Saboori:** Conceptualization, Project administration, Supervision, Validation, Writing – review & editing.

Declaration of competing interest

The authors declare that they have no known competing financial interests or personal relationships that could have appeared to influence the work reported in this paper.

Data availability

All data, models, and code generated or used during the study appear in the submitted article.

References

[1] I. Aiza, C. Baldi, F. Matías De La Vega, S. Sebastiani, N.E. Veronese, M. Yousefi, M. H. Mosallanejad, E. Maleki, M. Guagliano, L. Iuliano, A. Saboori, S. Bagherifard, Prog. Mater. Sci. 147 (2025) 101357.
[2] N. Li, S. Huang, G. Zhang, R. Qin, W. Liu, H. Xiong, G. Shi, J. Blackburn, Progress in additive manufacturing on new materials: a review, J. Mater. Sci. Technol. 35 (2) (2019) 242–269.
[3] M. Dadkhah, M.H. Mosallanejad, L. Iuliano, A. Saboori, A comprehensive overview on the latest progress in the additive manufacturing of metal matrix composites: potential, challenges, and feasible solutions, Acta Metall. Sin. 34 (2021) 1173–1200.
[4] A. Bandyopadhyay, K.D. Traxel, M. Lang, M. Juhasz, N. Eliaz, S. Bose, Alloy design via additive manufacturing: advantages, challenges, applications and perspectives, Mater. Today 52 (2022) 207–224.
[5] M.H. Mosallanejad, A. Abdi, F. Karpasand, N. Nassiri, L. Iuliano, A. Saboori, Additive manufacturing of titanium alloys: processability, properties, and applications, Adv. Eng. Mater. 25 (2023) 2301122.
[6] R. Ghanavati, H. Naffakh-Moosavy, Additive manufacturing of functionally graded metallic materials: a review of experimental and numerical studies, J. Mater. Res. Technol. 13 (2021) 1628–1664.
[7] ISO/ASTM TR 52912, Additive Manufacturing—Design—Functionally Graded Additive Manufacturing. https://www.iso.org/standard/71905.html, 2020.
[8] L. Yan, Y. Chen, F. Liou, Additive manufacturing of functionally graded metallic materials using laser metal deposition, Addit. Manuf. 31 (2020) 100901.
[9] D.R. Feenstra, R. Banerjee, H.L. Fraser, A. Huang, A. Molotnikov, N. Birbilis, Critical review of the state of the art in multi-material fabrication via directed energy deposition, Curr. Opinion Solid State Mater. Sci. 25 (4) (2021) 100924.
[10] C. Wei, L. Li, Recent progress and scientific challenges in multi-material additive manufacturing via laser-based powder bed fusion, Virtual Phys. Prototyp. 16 (3) (2021) 347–371.
[11] K. Shah, I. Ul Haq, A. Khan, S.A. Shah, M. Khan, A.J. Pinkerton, Parametric study of development of Inconel-steel functionally graded materials by laser direct metal deposition, Mater. Des. 54 (2014) 531–538 (1980–2015).
[12] J. Rodriguez, K. Hoefer, A. Haelsig, P. Mayr, Functionally graded SS 316L to Ni-based structures produced by 3D plasma metal deposition, Metals 9 (6) (2019) 620.
[13] J. Dutta Majumdar, I. Manna, Laser material processing, Int. Mater. Rev. 56 (5–6) (2011) 341–388.
[14] B.E. Carroll, R.A. Otis, J.P. Borgonia, J.O. Suh, R.P. Dillon, A.A. Shapiro, D. C. Hofmann, Z.K. Liu, A.M. Beese, Functionally graded material of 304L stainless steel and inconel 625 fabricated by directed energy deposition: characterization and thermodynamic modeling, Acta Mater. 108 (2016) 46–54.
[15] A. Reichardt, A.A. Shapiro, R. Otis, R.P. Dillon, J.P. Borgonia, B.W. McEnerney, P. Hosemann, A.M. Beese, Advances in additive manufacturing of metal-based functionally graded materials, Int. Mater. Rev. 66 (1) (2021) 1–29.
[16] X. Zhang, Y. Chen, F. Liou, Fabrication of SS316L-IN625 functionally graded materials by powder-fed directed energy deposition, Sci. Technol. Weld. Join. 24 (5) (2019) 504–516.
[17] X. Tong, C. Lu, Z. Huang, C. Zhang, F. Chen, Microstructures and mechanical properties of crack-free 316L stainless steel and Inconel 625 joint by using laser engineered net shaping, Opt. Laser Technol. 155 (2022) 108357.
[18] B. Chen, Y. Su, Z. Xie, C. Tan, J. Feng, Development and characterization of 316L/Inconel625 functionally graded material fabricated by laser direct metal deposition, Opt. Laser Technol. 123 (2020) 105916.
[19] Y. Su, B. Chen, C. Tan, X. Song, J. Feng, Influence of composition gradient variation on the microstructure and mechanical properties of 316 L/Inconel718 functionally graded material fabricated by laser additive manufacturing, J. Mater. Process. Technol. 283 (2020) 116702.
[20] D. Melzer, J. Džugan, M. Koukolíková, S. Rzepa, J. Vavřík, Structural integrity and mechanical properties of the functionally graded material based on 316L/IN718 processed by DED technology, Mater. Sci. Eng. A 811 (2021) 141038.
[21] K. Li, J. Zhan, M. Zhang, R. Ma, Q. Tang, D.Z. Zhang, L.E. Murr, H. Cao, A functionally graded material design from stainless steel to Ni-based superalloy by laser metal deposition coupled with thermodynamic prediction, Mater. Des. 217 (2022) 110612.
[22] J. Lu, W. Li, Improvement of tensile properties of laser directed energy deposited IN718/316L functionally graded material via different heat treatments, Mater. Sci. Eng. A 866 (2023) 144694.
[23] G. Xu, R. Wu, K. Luo, J. Lu, Effects of heat treatment on hot corrosion behavior of directed energy deposited In718/316L functionally graded material, Corros. Sci. 197 (2022) 110068.
[24] A. Hinojos, J. Mireles, A. Reichardt, P. Frigola, P. Hosemann, L.E. Murr, R. B. Wicker, Joining of Inconel 718 and 316 stainless steel using electron beam melting additive manufacturing technology, Mater. Des. 94 (2016) 17–27.
[25] S.M. Yusuf, X. Zhao, S. Yang, N. Gao, Interfacial characterisation of multi-material 316L stainless steel/Inconel 718 fabricated by laser powder bed fusion, Mater. Lett. 284 (2021) 128928.
[26] V. Errico, P. Posa, A. Fusco, A. Angelastro, S.L. Campanelli, Intralayer multi-material structure stainless-steel/nickel-superalloy fabricated via laser-powder bed fusion process, Manuf. Lett. 35 (2023) 11–15.
[27] Y. Wen, J. Gao, R.L. Narayan, P. Wang, L. Zhang, B. Zhang, U. Ramamurty, X. Qu, Microstructure-property correlations in as-built and heat-treated compositionally graded stainless steel 316L-Inconel 718 alloy fabricated by laser powder bed fusion, Mater. Sci. Eng. A 862 (2023) 144515.
[28] A.R. Kannan, S.M. Kumar, N.P. Kumar, N.S. Shanmugam, A.S. Vishnu, Y. Palguna, Process-microstructural features for tailoring fatigue strength of wire arc additive manufactured functionally graded material of SS904L and Hastelloy C-276, Mater. Lett. 274 (2020) 127968.
[29] T.S. Senthil, S.R. Babu, M. Puviyarasan, V. Dhinakaran, Mechanical and microstructural characterization of functionally graded Inconel 825-SS316L fabricated using wire arc additive manufacturing, J. Mater. Res. Technol. 15 (2021) 661–669.
[30] R. Sasikumar, A.R. Kannan, S.M. Kumar, R. Pramod, N.P. Kumar, N.S. Shanmugam, Y. Palguna, S. Sivankalai, Wire arc additive manufacturing of functionally graded material with SS 316L and IN625: microstructural and mechanical perspectives, CIRP J. Manuf. Sci. Technol. 38 (2022) 230–242.
[31] N. Chen, H.A. Khan, Z. Wan, J. Lippert, H. Sun, S.L. Shang, Z.K. Liu, J. Li, Microstructural characteristics and crack formation in additively manufactured bimetal material of 316L stainless steel and Inconel 625, Addit. Manuf. 32 (2020) 101037.
[32] A.A. Ferreira, O. Emadinia, J.M. Cruz, A.R. Reis, M.F. Vieira, Inconel 625/AISI 413 stainless steel functionally graded material produced by direct laser deposition, Materials 14 (19) (2021) 5595.

[33] S.H. Kim, H. Lee, S.M. Yeon, C. Aranas Jr., K. Choi, J. Yoon, S.W. Yang, H. Lee, Selective compositional range exclusion via directed energy deposition to produce a defect-free Inconel 718/SS 316L functionally graded material, Addit. Manuf. 47 (2021) 102288.
[34] S.W. Yang, J. Yoon, H. Lee, D.S. Shim, Defect of functionally graded material of inconel 718 and STS 316L fabricated by directed energy deposition and its effect on mechanical properties, J. Mater. Res. Technol. 17 (2022) 478–497.
[35] L. Xing, W. Quanjie, Z. Qirui, G. Yingchun, Z. Wei, Interface analyses and mechanical properties of stainless steel/nickel alloy induced by multi-metal laser additive manufacturing, J. Manuf. Process. 91 (2023) 53–60.
[36] X. Mei, X. Wang, Y. Peng, H. Gu, G. Zhong, S. Yang, Interfacial characterization and mechanical properties of 316L stainless steel/inconel 718 manufactured by selective laser melting, Mater. Sci. Eng. A 758 (2019) 185–191.
[37] W.W. Wits, E. Amsterdam, Graded structures by multi-material mixing in laser powder bed fusion, CIRP Ann. 70 (1) (2021) 159–162.
[38] W.Y. Chen, X. Zhang, M. Li, R. Xu, C. Zhao, T. Sun, Laser powder bed fusion of Inconel 718 on 316 stainless steel, Addit. Manuf. 36 (2020) 101500.
[39] T. Li, Z. Wang, S. Hu, Z. Yang, Y. Wang, Hot cracking during the fabrication of Inconel 625/stainless steel 308 L functionally graded material by dual-wire arc additive manufacturing, J. Manuf. Process. 82 (2022) 461–473.
[40] F. Mazzucato, D. Forni, A. Valente, E. Cadoni, Laser metal deposition of Inconel 718 alloy and as-built mechanical properties compared to casting, Materials 14 (2) (2021) 437.
[41] R. Ghanavati, H. Naffakh-Moosavy, M. Moradi, Additive manufacturing of thin-walled SS316L-IN718 functionally graded materials by direct laser metal deposition, J. Mater. Res. Technol. 15 (2021) 2673–2685.
[42] R. Ghanavati, H. Naffakh-Moosavy, M. Moradi, E. Gadalińska, A. Saboori, Residual stresses and distortion in additively-manufactured SS316L-IN718 multi-material by laser-directed energy deposition: a validated numerical-statistical approach, J. Manuf. Process. 108 (2023) 292–309.
[43] A. Saboori, A. Aversa, F. Bosio, E. Bassini, E. Librera, M. De Chirico, S. Biamino, D. Ugues, P. Fino, M. Lombardi, An investigation on the effect of powder recycling on the microstructure and mechanical properties of AISI 316L produced by directed energy deposition, Mater. Sci. Eng. A 766 (2019) 138360.
[44] R. Ghanavati, H. Naffakh-Moosavy, M. Moradi, M. Eshraghi, Printability and microstructure of directed energy deposited SS316l-IN718 multi-material: numerical modeling and experimental analysis, Sci. Rep. 12 (1) (2022) 16600.
[45] S.K. Nandi, A. Matthews, P.J. Withers, J. Stermsek, C. Fuchs, S. Roy, I. Manna, Functionally graded Tribaloy™ T800 and austenitic stainless steel by laser additive manufacturing, Mater. Today Commun. 39 (2024) 109274.
[46] J.S. Zuback, G.L. Knapp, T.A. Palmer, T. DebRoy, Deposit geometry and oxygen concentration spatial variations due to composition change in printed functionally graded components, Int. J. Heat Mass Transf. 164 (2021) 120526.
[47] N. Sargent, Y. Wang, D. Li, Y. Zhao, X. Wang, W. Xiong, Exploring alloy design pathway through directed energy deposition of powder mixtures: a study of stainless steel 316L and Inconel 718, Addit. Manuf. Lett. 6 (2023) 100133.
[48] R. Ghanavati, E. Lannunziata, E. Norouzi, S. Bagherifard, L. Iuliano, A. Saboori, Design and development of SS316L-IN718 functionally graded materials via laser powder bed fusion, Mater. Lett. 349 (2023) 134793.